SLAC–PUB–5808
April 1992
(T/E)

Experimental W Boson Physics at Future e^+e^- Linear Colliders

Timothy L. Barklow

Stanford Linear Accelerator Center
Stanford University, Stanford, California 94309

Abstract

The study of triple and quartic gauge boson vertices will be the centerpiece of experimental W boson physics at the next generation e^+e^- linear collider. We examine the sensitivity of a $\sqrt{s} = 500$ GeV e^+e^- linear collider to anomalous structure in the $W^+W^-\gamma$ and W^+W^-Z vertices. These vertices are tested by observing the reactions $e^-\gamma \to \nu W^-$, $\gamma\gamma \to W^+W^-$, and $e^+e^- \to W^+W^-$. We also look at W^+W^- rescattering in $e^+e^- \to W^+W^-$ as a means to study $W^+W^- \to W^+W^-$.

1. Introduction

Remarkably little is known about the interactions of the electroweak gauge bosons with each other. There are two distinct aspects of these interactions which are of interest. First, the triple and quartic gauge boson vertices need to be tested for any structure beyond what is produced by Standard Model radiative corrections. Such anomalous structure would appear, for example, if the W and Z bosons were themselves composite objects. Second, gauge boson scattering processes such as $W^+W^- \to W^+W^-$ can help us understand the mechanism responsible for electroweak symmetry breaking. W^+W^- scattering processes can be studied at an e^+e^- collider either by radiating virtual W's off of the e^- and e^+, or by studying W^+W^- rescattering in $e^+e^- \to W^+W^-$.

The paper is organized as follows. We first review the formalism for the description of the general $W^+W^-\gamma$ and W^+W^-Z vertices. We then examine the limits that can be obtained on the $W^+W^-\gamma$ vertex parameters using the reactions $e^-\gamma \to \nu W^-$ and $\gamma\gamma \to W^+W^-$, where the photons are either Weiszacker-Williams photons or back-scattered laser photons. Next, we study how well the process $e^+e^- \to W^+W^-$ can set limits on the $W^+W^-\gamma$ and W^+W^-Z vertex coupling parameters, paying special attention to the problem of disentangling the $W^+W^-\gamma$ and W^+W^-Z vertices. Finally, we discuss how W^+W^- rescattering in the reaction $e^+e^- \to W^+W^-$ can be used to study $W^+W^- \to W^+W^-$ and how it

---

⋆ Work supported by Department of Energy contract DE–AC03–76SF00515.

Contributed to the 1st Workshop on Physics with Linear Colliders,
Saariselka, Finland, September 9-14, 1992.

might be used to distinguish between different strongly interacting Higgs models.

2. The Parameterization of the Triple Gauge Boson Vertices

We use the formalism of Ref. 1 to describe the general W^+W^-V vertex, where $V = \gamma, Z$. The effective Lagrangian for the general W^+W^-V vertex as given in Eq.(2.1) of Ref. 1 is:

$$\begin{aligned}\mathcal{L}_{WWV}/g_{WWV} = & i g_1^V (W^\dagger_{\mu\nu} W^\mu V^\nu - W^\dagger_\mu V_\nu W^{\mu\nu}) + i\kappa_V W^\dagger_\mu W_\nu V^{\mu\nu} \\ & + \frac{i\lambda_V}{m_W^2} W^\dagger_{\lambda\mu} W^\mu{}_\nu V^{\nu\lambda} - g_4^V W^\dagger_\mu W_\nu (\partial^\mu V^\nu + \partial^\nu V^\mu) \\ & + g_5^V \varepsilon^{\mu\nu\rho\sigma} (W^\dagger_\mu \overleftrightarrow{\partial}_\rho W_\nu) V_\sigma + i\tilde{\kappa}_V W^\dagger_\mu W_\nu \tilde{V}^{\mu\nu} \\ & + \frac{i\tilde{\lambda}_V}{m_W^2} W^\dagger_{\lambda\mu} W^\mu{}_\nu \tilde{V}^{\nu\lambda} \quad .\end{aligned} \tag{1}$$

The terms with the coupling parameters g_1^V, κ_V, λ_V separately conserve C, P, and T, while the others violate C or P, or both. We will concentrate in this article on measurements of the coupling parameters κ_γ, λ_γ, κ_Z, and λ_Z.

In the standard model, at tree-level, $g_1^\gamma = g_1^Z = 1$, $\kappa_\gamma = \kappa_Z = 1$ and all other coupling parameters in Eq. (1) are 0. There is currently much discussion in the literature[2,3] regarding the extent to which present day electroweak measurements, especially precision LEP measurements, constrain κ_V and λ_V. In order to set the stage for our discussion of the limits obtainable with the NLC, we quote the results of Kane *et al.*[2] who considered loop effects and unitarity constraints:

$$\begin{aligned}|\lambda_\gamma| \leq 0.6 \quad & |\kappa_\gamma - 1| \leq 1.0 \\ |\lambda_Z| \leq 0.6 \quad & -0.8 \leq \kappa_Z - 1 \leq 0.0\end{aligned}$$

where $\kappa_V - 1 \equiv \kappa_V - 1$. These authors also estimated that the SSC should achieve limits on λ_γ and κ_γ of

$$|\lambda_\gamma| \leq 0.02 \quad |\kappa_\gamma - 1| \leq 0.1$$

with 10 fb^{-1} and that it would be difficult to obtain any limit on λ_Z and κ_Z with the SSC.

3. $e^-\gamma \to \nu W^-$ and $\gamma\gamma \to W^+W^-$

The $W^+W^-\gamma$ vertex can be tested at an e^+e^- collider by observing the reactions $e^-\gamma \to \nu W^-$ and $\gamma\gamma \to W^+W^-$. The photons can be virtual photons emitted by the initial electron or positron in the reactions $e^+e^- \to e^+\nu W^-$ and $e^+e^- \to e^+e^-W^+W^-$. The photons can be beamstrahlung photons. Or, the photons can be laser photons that have been Compton scattered off the electron and/or positron bunches in the drift region between the last focusing quadrupole and the interaction point[4,5,6]. In this paper we will only consider virtual Weiszacker-Williams photons and laser photons; for a discussion of how beamstrahlung photons can be used to study $e^-\gamma \to \nu W^-$, see Ref. 7.

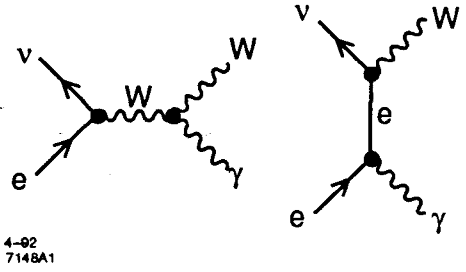

Fig. 1. The two Feynman diagrams for the reaction $e^-\gamma \to \nu W^-$.

Let us consider the reaction $e^-\gamma \to \nu W^-$. The idea of using this process to study the $W^+W^-\gamma$ vertex was discussed originally by Yehudai[7]. The final state is tagged using the decay of the W^- to a muon and a neutrino so that the event consists of a single muon in the detector and nothing else. The two tree-level Feynman diagrams for this process are shown in Fig. 1. The differential cross-section[8] as a function of $\cos\Theta$ is shown in in Fig. 2, where Θ is the angle between the final state W^- and initial state γ in the $e^-\gamma$ rest frame. Also shown in this figure is the dependence of the cross-section on the coupling parameters κ_γ and λ_γ.

The cross-section for $e^-\gamma \to \nu W^-$ at $\cos\Theta = -1$ is exactly zero in the standard model. However, it is not possible to accurately measure $\cos\Theta$ since the $e^-\gamma$ rest frame typically has a large boost with respect to the lab frame, and since the missing $\overline{\nu}_\mu$ smears the muon direction with respect to the W^- direction. Hence, it is not possible to take full advantage of the zero in the cross-section at $\cos\Theta = -1$. To set limits on κ_γ and λ_γ using this technique it is necessary to have a good measurement of the $e^-\gamma$ luminosity spectrum. Both the center-of-mass energy spectrum and the $e^-\gamma$ boost spectrum are required. The $e^-\gamma$ center-of-mass energy

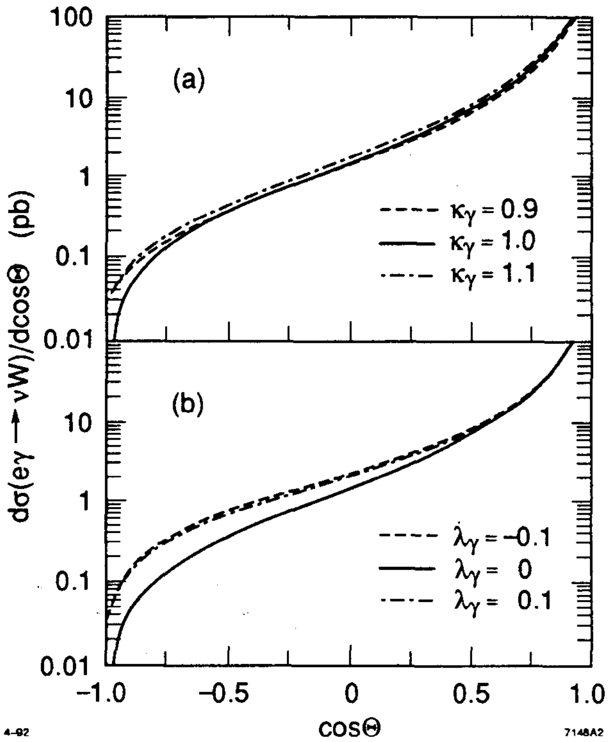

Fig. 2. The differential cross-section $d\sigma/\cos\Theta$ for $e^-\gamma \rightarrow \nu W^-$ with the standard model values for κ_γ and λ_γ, and for ±10% changes in these parameters.

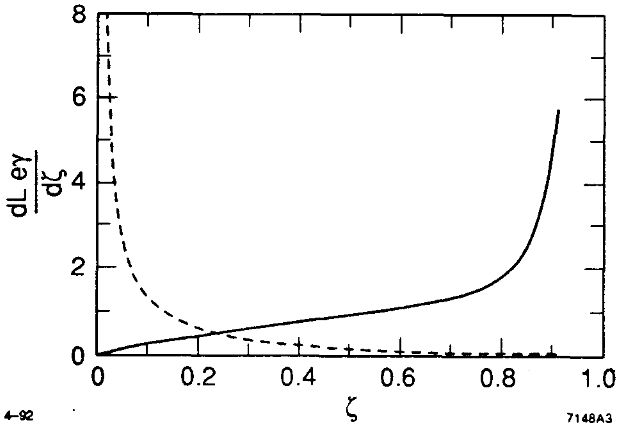

Fig. 3. The $e^-\gamma$ differential luminosity for virtual γ's (dashed line) and for Compton scattered laser photons (solid line).

luminosity spectra[8] is shown in Fig. 3 for virtual photons and for laser photons. The parameter ζ is defined by

$$\zeta \equiv \frac{M_{e\gamma}}{\sqrt{s}}$$

where $M_{e\gamma}$ is the $e^-\gamma$ center-of-mass energy and $\sqrt{s}$ is the e^+e^- center-of-mass energy. The spectra from Compton scattered laser photons is shown for the case where unpolarized laser photons are scattered off an unpolarized electron beam. The luminosity spectra would be measured using the process $e^-\gamma \to e^-\gamma$.

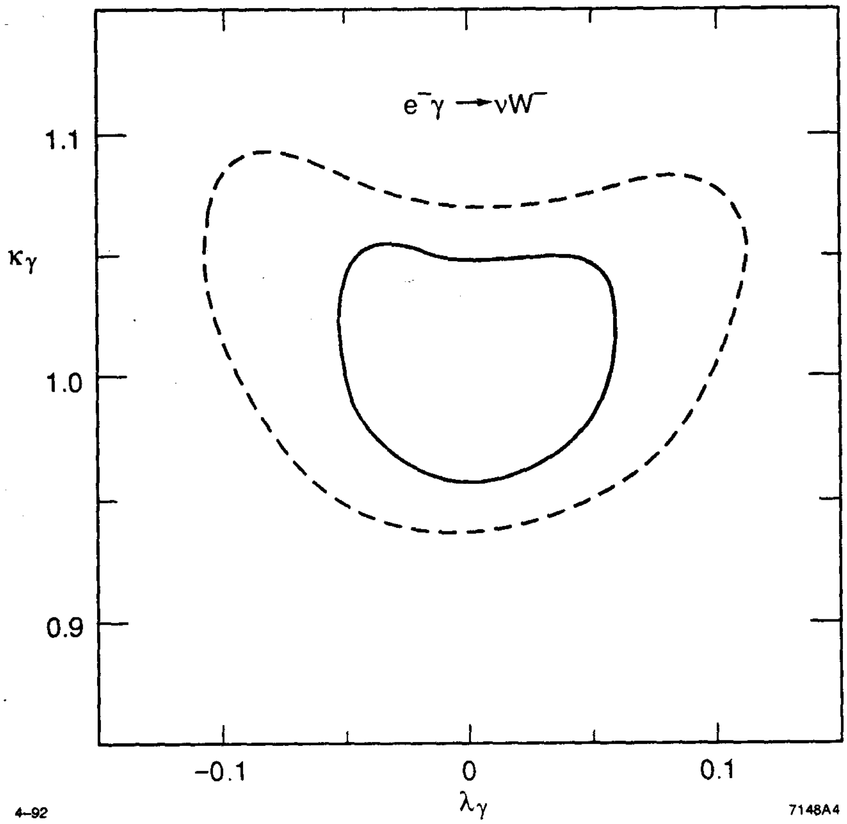

Fig. 4. 90% confidence level contours for $(\kappa_\gamma, \lambda_\gamma)$ from the reaction $e^-\gamma \to \nu W^-$ with classical bremmstrahlung photons (dotted contour) and back-scattered laser photons (solid contour).

Choi and Schrempp presented an analysis[8] at this conference in which they performed a least-squares fit of the differential cross-section as a function of $\cos\Theta$ and solved for κ_γ, λ_γ, and an overall normalization constant. The quantity which is actually measured by the detector is the muon momentum in the lab system. Therefore, in order to measure the W production angle Θ, the muon momentum distribution must be convoluted with a resolution function that includes detector resolution, detector boundary effects, the $e^-\gamma$ center-of-mass energy luminosity distribution, the $e^-\gamma$ system boost distribution, and the $W^- \to \mu^-\bar{\nu}$ decay distribution. Choi and Schrempp accounted for the effects of this convolution by applying a systematic error of 2% to the measurement of $\cos\Theta$. The 90% confidence level contours they obtained assuming an e^+e^- center-of-mass energy of 500 GeV and an e^+e^- luminosity of 10 fb^{-1} are shown in Fig. 4. Choi and Schrempp applied their fit using Weiszacker-Williams photons and using Compton scattered laser photons. We see that the Compton scattered laser photons produce a significant improvement in the excluded region. Yehudai[7,9] presented similar results at this conference.

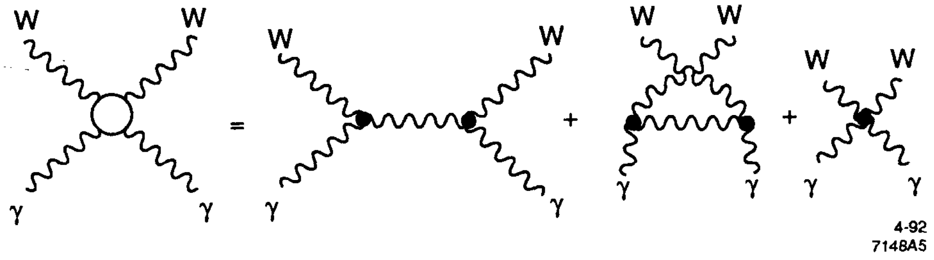

Fig. 5. The three tree-level Feynman diagrams for the process $\gamma\gamma \to W^+W^-$.

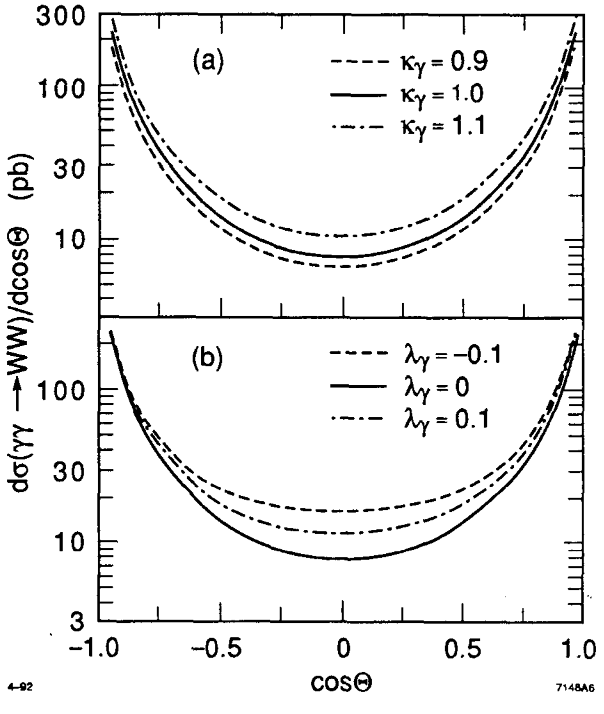

Fig. 6. The differential cross-section $d\sigma/\cos\Theta$ for $\gamma\gamma \to W^+W^-$ with the standard model values for κ_γ and λ_γ, and for ±10% changes in these parameters.

We now turn to the process $\gamma\gamma \to W^+W^-$. The three relevant tree-level diagrams are shown in Fig. 5. This process is potentially very interesting, since the first two diagrams each contain *two* $W^+W^-\gamma$ vertices and the last diagram has a single $W^+W^-\gamma\gamma$ four gauge boson vertex. The differential cross-section[8] is shown in Fig. 6.

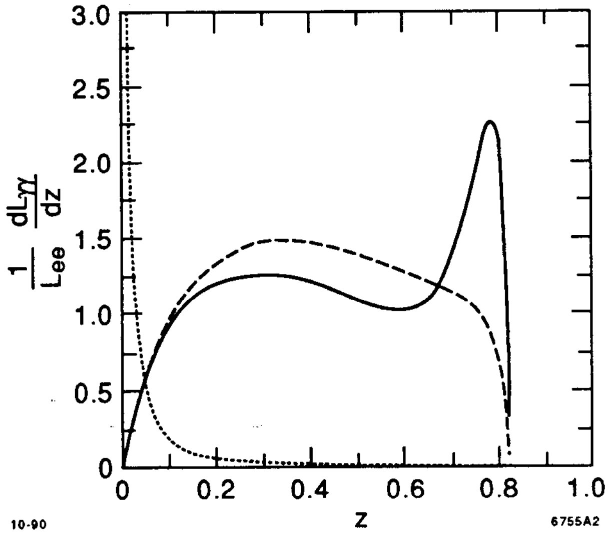

Fig. 7. Differential $\gamma\gamma$ luminosity for virtual $\gamma\gamma$ collisions (dotted line) and for backscattered laser photons with 0% e^- polarization (dashed line) and 90% e^- polarization (solid line).

The $\gamma\gamma$ luminosity is shown in Fig. 7. The quantity plotted is

$$\frac{1}{L_{ee}} \frac{dL_{\gamma\gamma}}{dz}$$

where L_{ee} is the e^+e^- (or e^-e^-) luminosity and $L_{\gamma\gamma}$ is the $\gamma\gamma$ luminosity. z is defined according to

$$z \equiv \frac{M_{\gamma\gamma}}{2E_b}$$

where $M_{\gamma\gamma}$ is the $\gamma\gamma$ invariant mass and E_b is the electron beam energy. The dotted line is the Weizsäcker–Williams spectrum for virtual $\gamma\gamma$ collisions. The dashed and solid lines show the backscattered laser luminosity spectrum for electron beam polarizations of 0% and 90%, respectively. In Fig. 7 we've assumed that the laser beams have 100% circular polarization, and that the helicities of the laser and electron beams have opposite signs. The $\gamma\gamma$ luminosity spectrum depends on the invariant mass of the electron and the laser photon. This invariant mass is often expressed in terms of the parameter x, defined by

$$x \equiv \frac{4E_b\omega_0}{m_e^2}$$

where ω_0 is the laser photon energy and m_e is the electron mass. The backscattered laser luminosity spectra in Fig. 7 is shown for $x = 4.82$.

The average helicities of the two photon beams depend strongly on $M_{\gamma\gamma}$ and on the relative polarizations of the laser and electron beams. However, the total cross-section for $\gamma\gamma \rightarrow W^+W^-$ does not show a strong depedence on $M_{\gamma\gamma}$, and Choi and Schrempp have concluded that polarized $\gamma\gamma$ beams do not signficantly improve the limits on κ_γ and λ_γ.

Although there might not be any advantage in giving the high energy photons a particular polarization, there might be an advantage in polarizing the e^- beams, because of the effect of e^- polarization on the $M_{\gamma\gamma}$ spectrum. For values of z greater than 0.7, the integrated $\gamma\gamma$ luminosity with 90% e^- polarization is more than two times the integrated luminosity with 0% e^- polarization. There are two motivations for shifting the $\gamma\gamma$ luminosity to larger values of z. First, much of the luminosity at small values of z is not useable because the W^+W^- system is boosted relative to the lab frame. Second, the sensitivity to anomalous values of κ_γ and λ_γ is improved as the W^+W^- center-of-mass energy is increased.

As was the case with $e^-\gamma \rightarrow \nu W^-$, we must take lab system observables and convert them into W^+W^- center-of-mass system variables in order to extract limits on κ_γ and λ_γ. However, it is not necessary to fold in the $\gamma\gamma$ center-of-mass and boost luminosity spectra when the W^+W^- final state is used (although ultimately it may be desirable to include this information). Since two W bosons are produced in the final state, there is sufficient information to reconstruct the center-of-mass system W^- production angle on an event-by-event basis. In fact, as was pointed out by F. Schrempp at this conference, the problem of reconstructing the center-of-mass system production and decay angles in $\gamma\gamma \rightarrow W^+W^-$ is equivalent to the problem of reconstructing the same variables in $e^+e^- \rightarrow W^+W^-$, once you allow for the possibility that both the e^+ and e^- can radiate photons. A discussion on how to reconstruct the W^+W^- center-of-mass system production and decay angles on an event-by-event basis will be postponed until the chapter on $e^+e^- \rightarrow W^+W^-$.

We now show the results on $\gamma\gamma \rightarrow W^+W^-$ that were contributed to this conference. Choi and Schrempp performed a least-squares fit of $d\sigma/\cos\Theta$, solving for κ_γ, λ_γ, and an overall normalization constant. As before, they accounted for all errors in the reconstruction of Θ by applying a systematic error of 2% to the measurement of $\cos\Theta$. The 90% confidence level contours they obtain assuming an e^+e^- center-of-mass energy of 500 GeV and an e^+e^- luminosity of 10 fb^{-1} are

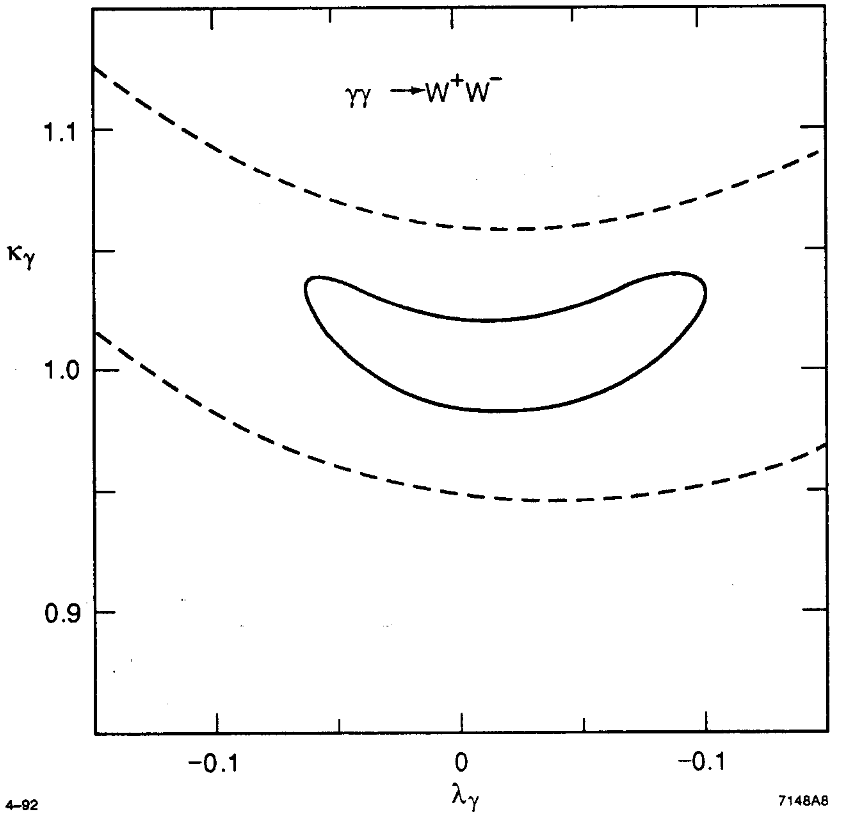

Fig. 8. 90% confidence level contours for $(\kappa_\gamma, \lambda_\gamma)$ from the reaction $\gamma\gamma \rightarrow W^+W^-$ with classical bremmstrahlung photons (dotted contour) and back-scattered laser photons (solid contour).

shown in Fig. 8. Compton scattered laser light provides an enormous advantage over Weiszacker-Williams photons when studying the reaction $\gamma\gamma \rightarrow W^+W^-$.

The results from Yehudai for both $\gamma\gamma \rightarrow W^+W^-$ and $e^-\gamma \rightarrow \nu W^-$ are shown in Fig. 9. Yehudai assumed Compton scattered laser photons as his photon source in this figure. The e^+e^- center-of-mass energy was 500 GeV and the e^+e^- luminosity was 10 fb^{-1}. A variety of different observables were used to obtain the 90 % confidence level contours.

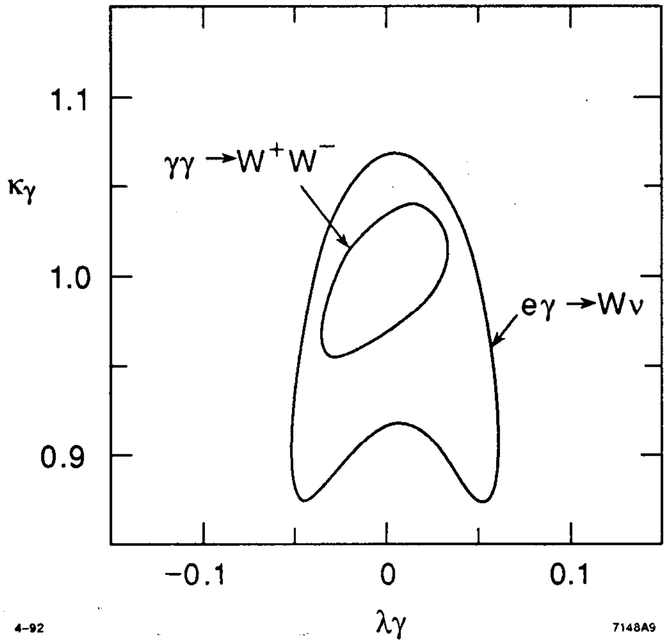

Fig. 9. 90% confidence level contours for $(\kappa_\gamma, \lambda_\gamma)$ from Ref. 10. The photons are Compton scattered laser photons.

4. $e^+e^- \rightarrow W^+W^-$

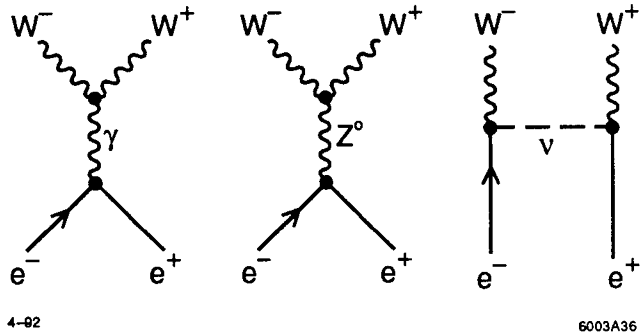

Fig. 10. The three tree-level Feynman diagrams for the process $e^+e^- \rightarrow W^+W^-$.

We start our discussion of $e^+e^- \rightarrow W^+W^-$ with some definitions. Following Ref. 1 we define our z-axis to be the direction of the W^- in the e^+e^- rest frame. The W^- production angle Θ is defined to be the angle between the initial state e^- and the W^- in the e^+e^- rest frame. The W^- and W^+ decay according to $W^- \rightarrow f_1\overline{f}_2$ and $W^+ \rightarrow f_3\overline{f}_4$. We define θ and ϕ to be the polar and azimuthal angles, respectively, of the fermion f_1 in the W^- rest frame, while $\overline{\theta}$ and $\overline{\phi}$ are the polar and azimuthal angles, respectively, of the anti-fermion $\overline{f}_4$ in the W^+ rest frame. We assume that the e^- beam has the polarization P_e where $P_e = 1$ is 100% right-handed and $P_e = -1$ is 100% left-handed.

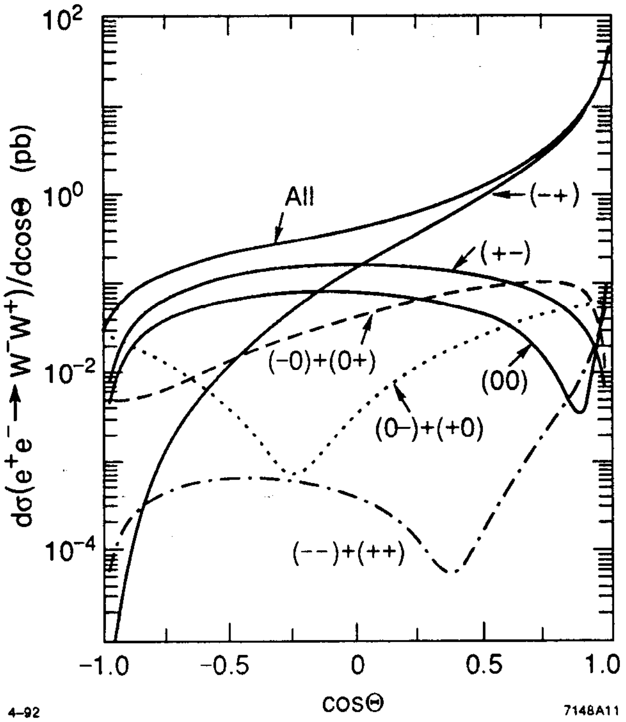

Fig. 11. The differential cross-section $d\sigma/\cos\Theta$ for $e^+e^- \rightarrow W^+W^-$ with the cross-section decomposed into different W^+W^- helicity combinations.

$e^+e^- \rightarrow W^+W^-$ proceeds through the three Feynman diagrams shown in Fig. 10. The differential cross-section $d\sigma/\cos\Theta$ is shown in Fig. 11, with the cross-section decomposed into different W^+W^- helicity combinations. Our notation is such that $(\lambda,\overline{\lambda})$ indicates that the W^- has helicity λ, the W^+ has helicity $\overline{\lambda}$, and that $\lambda = +, -, 0$ refers to right-handed transverse, left-handed transverse, and logitudinal W's, respectively. At forward angles the t-channel neutrino exchange diagram dominates and the cross-section consists almost entirely of left-handed transverse W^- and right-handed transverse W^+ gauge bosons. Transverse W's continue to dominate the cross-section at central angles. Only when $\cos\Theta$ drops below -0.9 do helicity combinations with at least one longitudinal gauge boson become important. The production angle θ therefore provides only limited information about individual W^+W^- helicity combinations.

The decay angles θ and ϕ can be used to improve the W^+W^- helicity analysis. To understand in detail how the decay angles reflect the helicity of the parent W we must look at the multi-differential cross-section for W^+W^- production and decay. The expression for the multi-differential cross-section depends on the event topology we are analyzing. Throughout this chapter we will concentrate on events where one W decays leptonically and the other decays hadronically. This topology has good statistics, can be separated from background with a high degree of purity, is rich in helicity information, and allows us to reconstruct all final state variables on an event-by-event basis. For events where the W^- decays leptonically and the W^+ decays hadronically (*topology A* events) the multi-differential cross section is given by:

$$\frac{d\sigma(\kappa_\gamma, \lambda_\gamma, \kappa_Z, \lambda_Z; \cos\Theta, \cos\theta, \phi, \cos\overline{\theta}, \overline{\phi}, P_e)}{d\cos\Theta \; d\cos\theta \; d\phi \; d\cos\overline{\theta} \; d\overline{\phi}} =$$

$$\frac{9\beta B_{lh}}{8192\pi^3 s} \sum_{\lambda,\lambda',\overline{\lambda},\overline{\lambda}'} \mathcal{Q}^{\lambda\overline{\lambda}}_{\lambda'\overline{\lambda}'}(\kappa_\gamma, \lambda_\gamma, \kappa_Z, \lambda_Z; \cos\Theta, P_e) \mathcal{D}^{\lambda}_{\lambda'}(\cos\theta, \phi) \overline{\mathcal{H}}^{\overline{\lambda}}_{\overline{\lambda}'}(\cos\overline{\theta}, \overline{\phi}) \tag{2}$$

where

$$\begin{aligned} \mathcal{Q}^{\lambda\overline{\lambda}}_{\lambda'\overline{\lambda}'} \equiv & (1 + P_e) \sum_{\overline{\sigma}} \mathcal{M}_1(+, \overline{\sigma}, \lambda, \overline{\lambda}; \Theta) \mathcal{M}_1^*(+, \overline{\sigma}, \lambda', \overline{\lambda}'; \Theta) \\ & + (1 - P_e) \sum_{\overline{\sigma}} \mathcal{M}_1(-, \overline{\sigma}, \lambda, \overline{\lambda}; \Theta) \mathcal{M}_1^*(-, \overline{\sigma}, \lambda', \overline{\lambda}'; \Theta) \quad . \end{aligned}$$

and

$$\overline{\mathcal{H}}^{\overline{\lambda}}_{\overline{\lambda}'}(\cos\overline{\theta}, \overline{\phi}) \equiv \left[\overline{\mathcal{D}}^{\overline{\lambda}}_{\overline{\lambda}'}(\cos\overline{\theta}, \overline{\phi}) + \overline{\mathcal{D}}^{\overline{\lambda}}_{\overline{\lambda}'}(-\cos\overline{\theta}, \overline{\phi} + \pi) \right] \quad .$$

The W^+W^- production amplitude $\mathcal{M}_1$, the W^- decay tensor $\mathcal{D}^{\lambda}_{\lambda'}$ and the W^+ decay tensor $\overline{\mathcal{D}}^{\overline{\lambda}}_{\overline{\lambda}'}$ are defined in Ref. 1. We note that

$$\mathcal{P}^{\lambda\overline{\lambda}}_{\lambda'\overline{\lambda}'} = \mathcal{Q}^{\lambda\overline{\lambda}}_{\lambda'\overline{\lambda}'} |_{P_e=0}$$

where $\mathcal{P}^{\lambda\overline{\lambda}}_{\lambda'\overline{\lambda}'}$ is the W^+W^- production tensor defined in Eq. 4.11 of Ref. 1. In Eq. (2), $\sqrt{s}$ is the e^+e^- center-of-mass energy, $\beta = \sqrt{1 - 4m_W^2/s}$ and B_{lh} is the product of the leptonic and hadronic branching ratios for the W boson. The sum $\overline{\mathcal{H}}^{\overline{\lambda}}_{\overline{\lambda}'}(\cos\overline{\theta}, \overline{\phi})$ appears in Eq. (2), instead of the single term $\overline{\mathcal{D}}^{\overline{\lambda}}_{\overline{\lambda}'}(\cos\overline{\theta}, \overline{\phi})$, because we assume that we cannot tag the flavor of the the quark jets in the decay of the W^+. When the W^+ decays leptonically and the W^- decays hadronically (*topology B*) we use the cross-section

$$\frac{d\overline{\sigma}(\kappa_\gamma,\lambda_\gamma,\kappa_Z,\lambda_Z;\cos\Theta,\cos\overline{\theta},\overline{\phi},\cos\theta,\phi,P_e)}{d\cos\Theta\; d\cos\theta\; d\phi\; d\cos\overline{\theta}\; d\overline{\phi}} =$$

$$\frac{9\beta B_{lh}}{8192\pi^3 s}\sum_{\lambda,\lambda',\overline{\lambda},\overline{\lambda}'}\mathcal{Q}^{\lambda\overline{\lambda}}_{\lambda'\overline{\lambda}'}(\kappa_\gamma,\lambda_\gamma,\kappa_Z,\lambda_Z;\cos\Theta,P_e)\mathcal{H}^{\lambda}_{\lambda'}(\cos\overline{\theta},\overline{\phi})\overline{\mathcal{D}}^{\overline{\lambda}}_{\overline{\lambda}'}(\cos\overline{\theta},\overline{\phi}) \tag{3}$$

where

$$\mathcal{H}^{\lambda}_{\lambda'}(\cos\overline{\theta},\overline{\phi}) \equiv \Big[\mathcal{D}^{\lambda}_{\lambda'}(\cos\theta,\phi)+\mathcal{D}^{\lambda}_{\lambda'}(-\cos\theta,\phi+\pi)\Big] \quad .$$

The W^- decay tensor $\mathcal{D}^{\lambda}_{\lambda'}(\cos\theta,\phi)$ is given explicitly by

$$\begin{aligned}
\mathcal{D}^{+}_{+} &= \frac{1}{2}(1-\cos\theta)^2, \qquad \mathcal{D}^{-}_{-} = \frac{1}{2}(1+\cos\theta)^2, \qquad \mathcal{D}^{0}_{0} = \sin^2\theta,\\
\mathcal{D}^{+}_{0} &= \frac{1}{\sqrt{2}}(1-\cos\theta)\sin\theta e^{i\phi},\\
\mathcal{D}^{-}_{0} &= -\frac{1}{\sqrt{2}}(1+\cos\theta)\sin\theta e^{-i\phi},\\
\mathcal{D}^{+}_{-} &= \frac{1}{2}\sin^2\theta e^{2i\phi},
\end{aligned} \tag{4}$$

and $\mathcal{D}^{\lambda'}_{\lambda} = (\mathcal{D}^{\lambda}_{\lambda'})^*$. We also show explicitly the expression for the W^- hadronic decay tensor $\mathcal{H}^{\lambda}_{\lambda'}(\cos\theta,\phi)$:

$$\begin{aligned}
\mathcal{H}^{+}_{+} &= 1+\cos^2\theta, \qquad \mathcal{H}^{-}_{-} = 1+\cos^2\theta, \qquad \mathcal{H}^{0}_{0} = 2\sin^2\theta,\\
\mathcal{H}^{+}_{0} &= \sqrt{2}\cos\theta\sin\theta e^{i\phi}\\
\mathcal{H}^{-}_{0} &= -\sqrt{2}\cos\theta\sin\theta e^{-i\phi}\\
\mathcal{H}^{+}_{-} &= \sin^2\theta e^{2i\phi} \quad .
\end{aligned} \tag{5}$$

Although the W^- hadronic decay tensor $\mathcal{H}^{\lambda}_{\lambda'}(\cos\theta,\phi)$ does not contain as much helicity information as the leptonic decay tensor $\mathcal{D}^{\lambda}_{\lambda'}(\cos\theta,\phi)$, its information content is nevertheless non-negligible.

The decay tensor components $\mathcal{D}^{+}_{+}$, $\mathcal{D}^{-}_{-}$, and $\mathcal{D}^{0}_{0}$ for pure left-handed transverse, pure right-handed transverse, and pure longitudinal W^- gauge bosons, respectively, have distinctive polar angle distributions, and do not exhibit an azimuthal angle dependence. Distributions in $d\sigma/\cos\theta$ are shown in Fig. 12 for various values of $\cos\Theta$. At $\cos\Theta = +0.5$ we can see from the $\cos\theta$ distribution that the W^- is almost entirely left-handed. On the other hand, at $\cos\Theta = 0$ and $\cos\Theta = -0.5$ the W^- is a mixture of various polarizations.

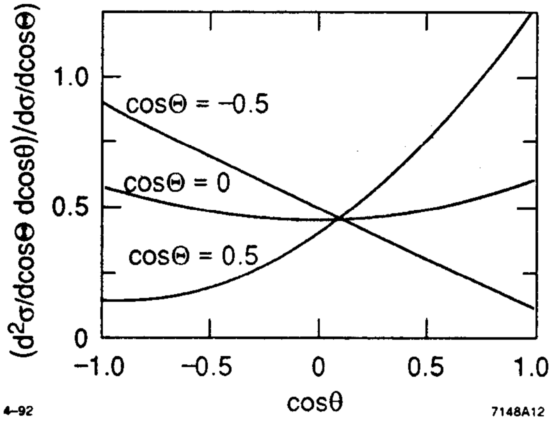

Fig. 12. Distributions in $d\sigma/\cos\theta$ for various values of $\cos\Theta$.

The interference terms in Eq. (4) do depend on the decay azimuthal angle. For example, the decay tensor component $\mathcal{D}_0^0$ for the pure longitudinal W^- boson is indistinguishable from the component $\mathcal{D}_-^+$ for the interference between left-handed and right-handed transverse W^- bosons, except for the azimuthal angle factor $e^{2i\phi}$. Our set of experimental observables therefore includes not only the cosines of the polar angles, $\cos\Theta$, $\cos\theta$, and $\cos\overline{\theta}$, but also the azimuthal angles ϕ and $\overline{\phi}$. Our full helicity analysis then consists of a maximum likelihood fit of the form

$$\begin{aligned} &\ln L(\kappa_\gamma, \lambda_\gamma, \kappa_Z, \lambda_Z; \mathcal{L}_k) = \\ &\sum_{i_1=1}^{N_\Theta}\sum_{i_2=1}^{N_\theta}\sum_{i_3=1}^{N_\phi}\sum_{i_4=1}^{N_{\overline{\theta}}}\sum_{i_5=1}^{N_{\overline{\phi}}}\sum_{k=1}^{N_{P_e}} \Big[r_{i_1i_2i_3i_4i_5k}\ln(\mu_{i_1i_2i_3i_4i_5k}) - \mu_{i_1i_2i_3i_4i_5k} \\ &\qquad + \overline{r}_{i_1i_2i_3i_4i_5k}\ln(\overline{\mu}_{i_1i_2i_3i_4i_5k}) - \overline{\mu}_{i_1i_2i_3i_4i_5k}\Big] \end{aligned} \tag{6}$$

where $r_{i_1i_2i_3i_4i_5k}$ and $\mu_{i_1i_2i_3i_4i_5k}$ are the measured number of topology A events and the expected number of topology A events, respectively, in the bin centered at $\cos\Theta_{i_1}$, $\cos\theta_{i_2}$, ϕ_{i_3}, $\cos\overline{\theta}_{i_4}$, $\overline{\phi}_{i_5}$, when the e^- polarization is P_{ek}. $\overline{r}_{i_1i_2i_3i_4i_5k}$ and $\overline{\mu}_{i_1i_2i_3i_4i_5k}$ are the measured and expected number of topology B events. The volume of a bin is

$$\Delta\Omega = \frac{16\pi^2}{N_\Theta N_\theta N_\phi N_{\overline{\theta}} N_{\overline{\phi}}} \quad .$$

We define $\mu_{i_1i_2i_3i_4i_5k}$ as follows:

$$\mu_{i_1 i_2 i_3 i_4 i_5 k}(\kappa_\gamma, \lambda_\gamma, \kappa_Z, \lambda_Z, \mathcal{L}_k) \equiv \mathcal{L}_k \int\limits_{\eta_{i_1}^-}^{\eta_{i_1}^+} \mathrm{d}\cos\Theta \int\limits_{\eta_{i_2}^-}^{\eta_{i_2}^+} \mathrm{d}\cos\theta \int\limits_{\eta_{i_3}^-}^{\eta_{i_3}^+} \mathrm{d}\phi \int\limits_{\eta_{i_4}^-}^{\eta_{i_4}^+} \mathrm{d}\cos\overline{\theta} \int\limits_{\eta_{i_5}^-}^{\eta_{i_5}^+} \mathrm{d}\overline{\phi}$$

$$\left\{ \frac{\mathrm{d}\xi(\cos\Theta, \cos\theta, \phi, \cos\overline{\theta}, \overline{\phi}, P_{ek})}{\mathrm{d}\cos\Theta\ \mathrm{d}\cos\theta\ \mathrm{d}\phi\ \mathrm{d}\cos\overline{\theta}\ \mathrm{d}\overline{\phi}} + \left[\int\limits_{-1}^{1} \mathrm{d}\cos\Theta' \int\limits_{-1}^{1} \mathrm{d}\cos\theta' \int\limits_{0}^{2\pi} \mathrm{d}\phi' \int\limits_{0}^{1} \mathrm{d}\cos\overline{\theta}' \int\limits_{0}^{2\pi} \mathrm{d}\overline{\phi}' \right.\right.$$

$$G(\cos\Theta, \cos\theta, \phi, \cos\overline{\theta}, \overline{\phi}; \cos\Theta', \cos\theta', \phi', \cos\overline{\theta}', \overline{\phi}')$$

$$\left.\left. \cdot \frac{\mathrm{d}\sigma(\kappa_\gamma, \lambda_\gamma, \kappa_Z, \lambda_Z; \cos\Theta', \cos\theta', \phi', \cos\overline{\theta}', \overline{\phi}', P_{ek})}{\mathrm{d}\cos\Theta'\ \mathrm{d}\cos\theta'\ \mathrm{d}\phi'\ \mathrm{d}\cos\overline{\theta}'\ \mathrm{d}\overline{\phi}'} \right] \right\}$$

where

$$\eta_{i_1}^{\pm} = \cos\Theta_{i_1} \pm \frac{1}{N_\Theta}; \qquad \eta_{i_2}^{\pm} = \cos\theta_{i_2} \pm \frac{1}{N_\theta}; \qquad \eta_{i_3}^{\pm} = \phi_{i_3} \pm \frac{\pi}{N_\phi}$$

$$\eta_{i_4}^{\pm} = \cos\overline{\theta}_{i_4} \pm \frac{1}{2N_{\overline{\theta}}}; \qquad \eta_{i_5}^{\pm} = \overline{\phi}_{i_5} \pm \frac{\pi}{N_{\overline{\phi}}}$$

and

$$\frac{\mathrm{d}\xi(\cos\Theta, \cos\theta, \phi, \cos\overline{\theta}, \overline{\phi}, P_e)}{\mathrm{d}\cos\Theta\ \mathrm{d}\cos\theta\ \mathrm{d}\phi\ \mathrm{d}\cos\overline{\theta}\ \mathrm{d}\overline{\phi}}$$

is the multi-differential cross-section for background processes that pass all the W^+W^- analysis cuts. The function

$$G(\cos\Theta, \cos\theta, \phi, \cos\overline{\theta}, \overline{\phi}; \cos\Theta', \cos\theta', \phi', \cos\overline{\theta}', \overline{\phi}')$$

is the resolution function for our $e^+e^- \to W^+W^-$ analysis. It is defined so that $G\mathrm{d}\Omega$ is the probability that a W^+W^- pair produced with the variables

$$\cos\Theta', \cos\theta', \phi', \cos\overline{\theta}', \text{ and } \overline{\phi}'$$

passes all the W^+W^- analysis cuts and is placed in a bin of volume $\mathrm{d}\Omega$ centered at

$$\cos\Theta, \cos\theta, \phi, \cos\overline{\theta}, \overline{\phi}\ .$$

We shall assume that the W^+W^- final state can be isolated sufficiently well that

$$\frac{\mathrm{d}\xi(\cos\Theta, \cos\theta, \phi, \cos\overline{\theta}, \overline{\phi}, P_e)}{\mathrm{d}\cos\Theta\ \mathrm{d}\cos\theta\ \mathrm{d}\phi\ \mathrm{d}\cos\overline{\theta}\ \mathrm{d}\overline{\phi}} = 0,$$

is a good approximation. Although we are confident that this indeed is a good approximation, it remains an important topic of future study to actually prove that this will be the case.

For most of the results that are presented in this chapter we assume that there is no initial state radiation, beamstrahlung or intrinsic linac energy spread. Furthermore, we assume that we have a perfect detector that can measure the variables $\cos\Theta, \cos\theta, \phi, \cos\overline{\theta}, \overline{\phi}$ with 100% efficiency and infinite accuracy for topology A and B events with $|\cos\Theta| < 0.8$:

$$G(\Omega;\Omega') = \begin{cases} \delta^5(\Omega;\Omega'), & \text{if } |\cos\Theta| < 0.8; \\ 0, & \text{otherwise,} \end{cases}$$

where we have used Ω to denote the set of variabes $\cos\Theta$, $\cos\theta$, ϕ, $\cos\overline{\theta}$, and $\overline{\phi}$. We shall also assume for most of this chapter that $G(\Omega;\Omega') = 0$ for topology A and B events in which the W decays via $W \rightarrow \tau\nu$. The only source of error remaining after we make these assumptions is the statistical error associated with each bin count. At the end of the chapter we shall discuss how initial state radiation and beamstrahlung might be dealt with, and we investigate how our results are changed once detector resolution and $W \rightarrow \tau\nu$ decays are incorporated into a realistic resolution function.

We first fix κ_Z and λ_Z at their standard model values and do a three parameter log-likelihood fit of κ_γ, λ_γ, and $\mathcal{L}$. Here, and throughout this chapter, we use a binning of

$$N_\Theta = 20 \quad \text{and} \quad N_\theta = N_\phi = N_{\overline{\theta}} = N_{\overline{\phi}} = 5\ .$$

This choice was driven by computer CPU and memory considerations. We don't know if a a finer binning granularity can improve our results. Fig. 13 shows 95% confidence level contours for three different center-of-mass energies. The luminosities of 1.3 fb^{-1} at $\sqrt{s} = 200$ GeV, 10 fb^{-1} at $\sqrt{s} = 500$ GeV, and 44 fb^{-1} at $\sqrt{s} = 1000$ GeV were chosen to give roughly 4100 detected events at each of the three center-of-mass energies. Fig. 13(a) shows the 95% confidence level contours for $\sqrt{s} = 200$ GeV and $\sqrt{s} = 500$ GeV; the contour for $\sqrt{s} = 1000$ GeV is too small to appear on this scale. Also shown in Fig. 13(a) is an estimate^2 of the 95% confidence level contour for the SSC at 10 fb^{-1}. There is a significant improvement in the limits in going from $\sqrt{s} = 200$ GeV to $\sqrt{s} = 500$ GeV. Note that the 95% confidence limits from a $\sqrt{s} = 500$ GeV e^+e^- collider at 10 fb^{-1} are much better than the limits estimated in Ref. 2 for the SSC at 10 fb^{-1}. Fig. 13(b) shows the 95% confidence level contour for $\sqrt{s} = 500$ GeV in more detail, and it also shows the contour for $\sqrt{s} = 1000$ GeV. We can see that the individual bounds on κ_γ and λ_γ at $\sqrt{s} = 500$ GeV are $|\kappa_\gamma - 1|, \lambda_\gamma < 0.01$.

Next, we allow all four of our couplings parameters to be free as we perform a six parameter maximum log-likelihood fit of $\kappa_\gamma, \lambda_\gamma, \kappa_Z, \lambda_Z, \mathcal{L}_+, \mathcal{L}_-$. The symbols $\mathcal{L}_+$ and $\mathcal{L}_-$ refer to the luminosities of two runs at different e^- polarizations. We

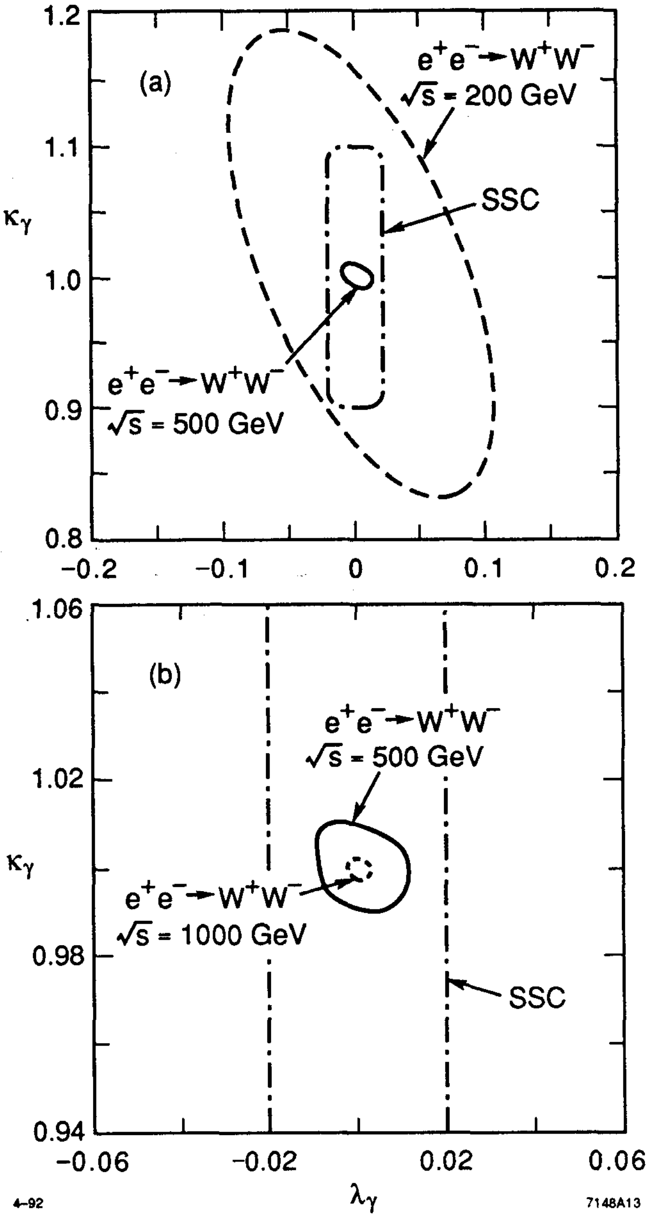

Fig. 13. Projection onto the $(\kappa_\gamma, \lambda_\gamma)$ plane of the 95% confidence level joint probability ellipsoid for a three-parameter maximum likelihood fit of $\kappa_\gamma, \lambda_\gamma, \mathcal{L}$. Standard model values are assumed for κ_Z and λ_Z. Projections for e^+e^- colliders with 1.3 fb^{-1} at $\sqrt{s}$ = 200 GeV, 10 fb^{-1} at $\sqrt{s}$ = 500 GeV, and 44 fb^{-1} at $\sqrt{s}$ = 1000 GeV are plotted, as well as an estimate of the limits from the SSC with 10 fb^{-1} (the SSC limit is independent of κ_Z and l_Z).

will first assume that $P_e = 0$ for both of these runs and that $\mathcal{L}_+ = \mathcal{L}_- = 5\ fb^{-1}$. The projection onto the $(\kappa_\gamma, \lambda_\gamma)$ and (κ_Z, λ_Z) planes of the six-dimensional 95% confidence level joint probability ellipsoid is shown in Fig. 14. The two-dimensional projection of the six-dimensional ellipsoid is not a nice contour, presumably be-

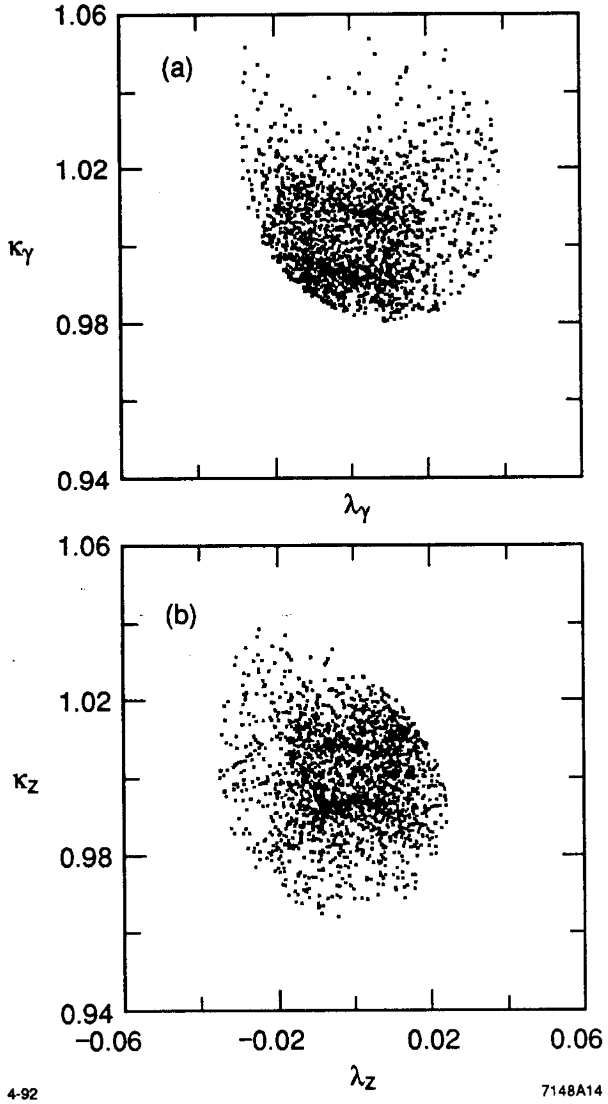

Fig. 14. Projection onto the (a) $(\kappa_\gamma, \lambda_\gamma)$ plane and (b) (κ_Z, λ_Z) plane of the 95% confidence level joint probability ellipsoid for a six parameter maximum likelihood fit of $\kappa_\gamma, \lambda_\gamma, \kappa_Z, \lambda_Z, \mathcal{L}_+, \mathcal{L}_-$. Unpolarized beams are assumed with $\mathcal{L}_+ + \mathcal{L}_- = 10\ fb^{-1}$ at $\sqrt{s} = 500$ GeV.

cause the shape of the six-dimensional object is so complicated. Each point is generated by first choosing a direction at random in the six-dimensional space, then traveling in this direction from the standard model point to the surface of the 95% confidence level ellipsoid, and finally projecting this point onto the plane. We interpret the outer boundary of the set of points in Fig. 14(a) to be the 95% confidence level contour for κ_γ and λ_γ, independent of κ_Z and λ_Z. If we compare Figs. 13(b) and 14(a) we see that our individual bounds on κ_γ and λ_γ are degraded by a factor of about five when we allow all four of our coupling parameters to vary.

The individual bounds on κ_γ and λ_γ are now $|\kappa_\gamma - 1|, \lambda_\gamma < 0.05$. Comparing Figs. 14(a) and (b) we see that the area of the excluded region in (κ_Z, lz) space is roughly the same as the excluded area in $(\kappa_\gamma, \lambda_\gamma)$ space.

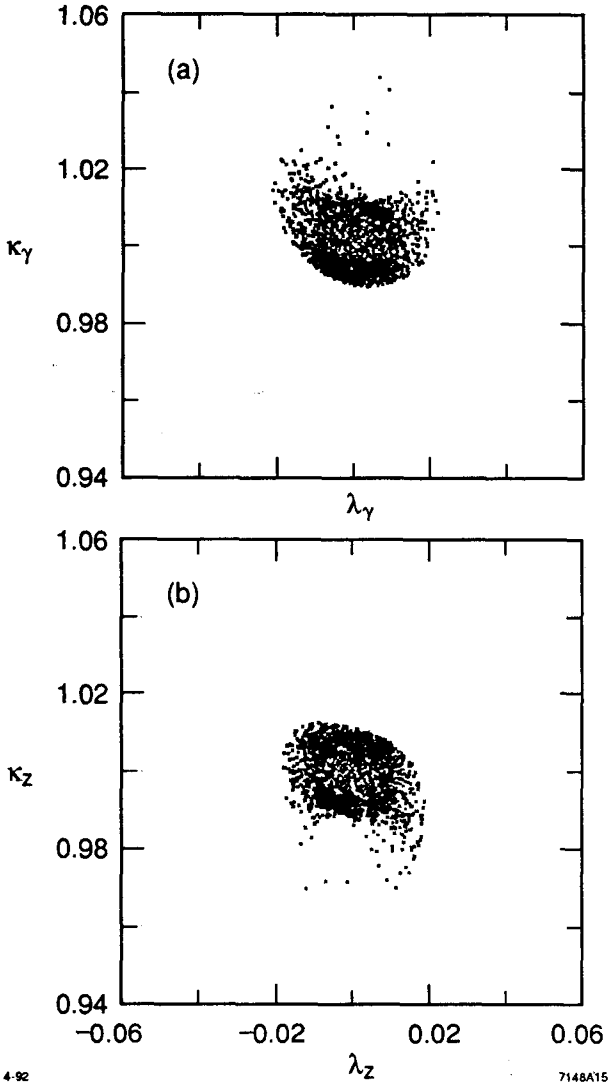

Fig. 15. Projection onto the (a) $(\kappa_\gamma, \lambda_\gamma)$ plane and (b) (κ_Z, λ_Z) plane of the 95% confidence level joint probability ellipsoid for a six-parameter maximum likelihood fit of $\kappa_\gamma, \lambda_\gamma, \kappa_Z, \lambda_Z, \mathcal{L}_+, \mathcal{L}_-$. The data set consisted of $\mathcal{L}_+ = 5\ fb^{-1}$ of 90% right-handed electrons and $\mathcal{L}_- = 5\ fb^{-1}$ of 90% left-handed electrons at $\sqrt{s} = 500$ GeV.

Given that the e^+e^-Z vertex is parity violating while the $e^+e^-\gamma$ vertex is parity conserving, it might seem plausible that polarized electron beams could help separate anomalous κ_γ and λ_γ values from anomalous κ_Z and λ_Z values.

This indeed is the case. In Fig. 15 we show the projections of the six-dimensional 95% confidence level joint probability ellipsoid assuming that $\mathcal{L}_+ = 5\ fb^{-1}$ is collected with 90% right-handed electrons and $\mathcal{L}_- = 5\ fb^{-1}$ is collected with 90% left-handed electrons, all at $\sqrt{s} = 500$ GeV. $\kappa_\gamma - 1$ and λ_γ are now each bounded by ± 0.2 .

We now discuss how the the variables $\cos\Theta$,$\cos\theta$,ϕ,$\cos\overline{\theta}$, and $\overline{\phi}$ can be measured in the presence of effects such as initial state radiation, beamstrahlung, detector resolution and W decays to tau leptons. We first discuss beamstrahlung, initial state radiation, and linac energy spread. Beamstrahlung, initial state radiation, and linac energy spread cause the e^- and e^+ to lose a certain amount of energy before they annihilate. We shall simply refer to this energy loss as initial state radiation, or ISR, even though the energy loss arises from a combination of the three mechanisms.

There are a variety of ways to handle ISR. In one approach the W^+W^- helicity analysis is performed as if there was no ISR and all the effects of ISR are included in the resolution function $G(\Omega,\Omega')$. In the other extreme, cuts are imposed to produce a sample of events with no ISR, and the resolution function then does not depend on any of the ISR energy loss mechanisms. The former approach suffers from having a more complicated resolution function which includes a double differential luminosity distribution that must be measured using Bhabhas. The former approach also has the disadvantage that the W^+W^- final state is analyzed over a wide range of W^+W^- center-of-mass values. The latter approach, on the other hand, will suffer from smaller statistics. We opt for the latter approach, if for no other reason than that it is easier to implement in a short period of time. It is not clear that some combination of the two approaches will not ultimately yield the greatest precision.

We model ISR by assuming that the initial state electron and positron radiate photons of energy E_{γ^-} and E_{γ^+}, respectively. Recall that we are dealing with W^+W^- events in which one W decays leptonically and the other decays hadronically. If we measure $\vec{p}_l$, the momentum of the charged lepton from the leptonically decaying W, and $\vec{\beta}_H$, the velocity of the hadronically decaying W, then we have enough information to solve for E_{γ^-} and E_{γ^+}. In the process we also solve for $\vec{p}_\nu$, the momentum of the neutrino from the leptonically decaying W. The velocity of the hadronically decaying W is defined by

$$\vec{\beta}_H \equiv \frac{\vec{p}_H^{\,0}}{E_H^0}$$

where E_H^0 and $\vec{p}_H^{\,0}$ are the measured energy and measured momentum, respectively, of the hadronically decaying W.

To solve for $E_{\gamma^-}, E_{\gamma^+}$, and $\vec{p}_\nu$ we use the four energy-momentum constraints and the constraint that the the charged lepton and the neutrino form a system with an invariant mass equal to the W boson mass:

$$\begin{aligned}
E_{\gamma^-} + E_{\gamma^+} + \frac{M_W}{\sqrt{1-\beta_H^2}} + E_l + \sqrt{\vec{p}_\nu^{\,2}} &= \sqrt{s} \\
\frac{M_W}{\sqrt{1-\beta_H^2}}\beta_{H_x} + p_{l_x} + p_{\nu_x} &= 0 \\
\frac{M_W}{\sqrt{1-\beta_H^2}}\beta_{H_y} + p_{l_y} + p_{\nu_y} &= 0 \\
E_{\gamma^-} - E_{\gamma^+} + \frac{M_W}{\sqrt{1-\beta_H^2}}\beta_{H_z} + p_{l_z} + p_{\nu_z} &= 0 \\
\left(E_l + \sqrt{\vec{p}_\nu^{\,2}}\right)^2 - (\vec{p}_l + \vec{p}_\nu)^2 &= M_W^2
\end{aligned} \tag{7}$$

There are two solutions to Eq. (7), and it is not always possible to determine which solution is the correct one. This is not a problem, however, as most events with ISR can be removed by requiring that there be at least one solution to Eq. (7)with

$$0.98 < \frac{M_{WW}}{\sqrt{s}} < 1.1 \tag{8}$$

where M_{WW} is the reconstructed invariant mass of the W^+W^- system.

We simulate detector effects with a fast Monte Carlo program for the SLD detector[11]. To build a clean sample of Topology A and B events we first require that an event have at least one identified electron or muon. For each identified charged lepton i we calculate M_i, the mass of all charged and neutral tracks excluding the charged lepton i. The charged lepton with the smallest value of $|M_i - M_W|$ is taken to be the charged lepton from the leptonically decaying W. We then require that $|M_i - M_W| < 20$ GeV. At this point we have all the information we need to calculate the two solutions to Eq. (7). Our final cut is then Eq. (8). For events where the W^- is the leptonically decaying W it is straightforward to calculate $\cos\theta$, and ϕ. We perform a thrust analysis in the rest frame of the hadronically decaying W to calculate $\cos\overline{\theta}$ and $\overline{\phi}$.

The resolution function $G(\Omega;\Omega')$ is constructed by passing W^+W^- Monte Carlo events with topologies A and B through the fast SLD detector simulation and then subjecting the events to the above cuts. Monte Carlo events with $W \rightarrow \tau\nu$, are included so that W decays to taus are accounted for. If the resolution function

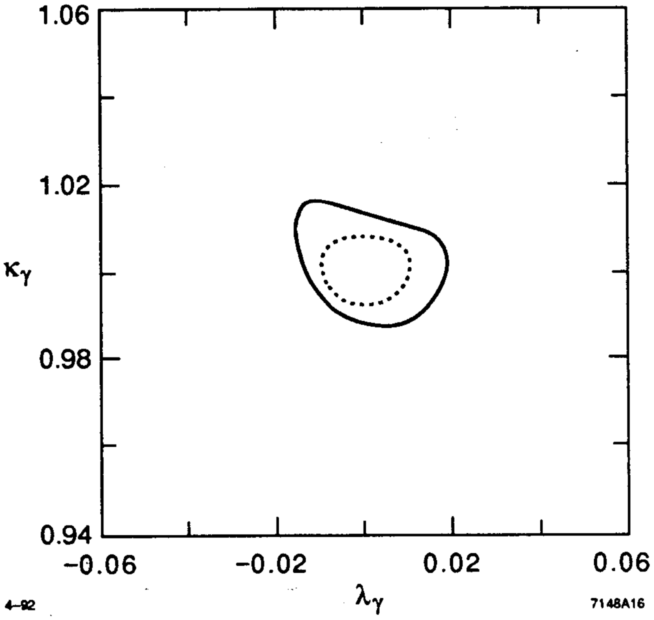

Fig. 16. Projection onto the $(\kappa_\gamma, \lambda_\gamma)$ plane of the 95% confidence level joint probability ellipsoid for a three-parameter maximum likelihood fit of $\kappa_\gamma, \lambda_\gamma, \mathcal{L}$ with a realistic resolution function. Standard model values are assumed for κ_Z and λ_Z. The luminosities of 10 fb^{-1} (solid curve) and 24 fb^{-1} (dotted curve) are taken at $\sqrt{s} = 500$ GeV.

is in the form of a matrix, care must be taken that the granularity of the resolution function binning near the boundaries of the detector is sufficiently fine.

Fig. 16 shows what happens to our $(\kappa_\gamma, \lambda_\gamma)$ limits when we use our realistic resolution function. As in Fig. 13(b), 95% confidence level contours are plotted for the three parameter fit of $\kappa_\gamma, \lambda_\gamma, \mathcal{L}$, keeping κ_Z and λ_Z fixed at their standard model values. The solid curve in Fig. 16 is for $\mathcal{L} = 10\ fb^{-1}$ and we see that it is signficantly wider than the $\mathcal{L} = 10\ fb^{-1}$ curve of Fig. 13(b). However, only 1700 events passed our cuts with $\mathcal{L} = 10\ fb^{-1}$. If we increase the luminosity from 10 fb^{-1} to 24 fb^{-1} then we again have 4100 detected events, and our 95% confidence level contour (dotted curve) is as good as the the contour in Fig. 13(b). This demonstrates, for example, that a detector with the resolution specifications of the SLD is good enough to do the W^+W^- physics described in this article.

5. W^+W^- Rescattering in $e^+e^- \to W^+W^-$

Final state rescattering in $e^+e^- \to W^+W^-$, shown diagramatically in Fig. 17, can give us information about the $J = 1$ partial wave in the scattering process

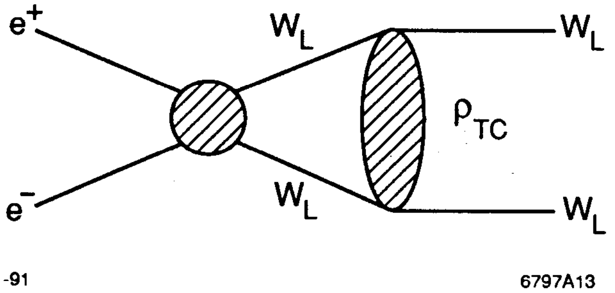

Fig. 17. Final state rescattering in $e^+e^- \rightarrow W^+W^-$

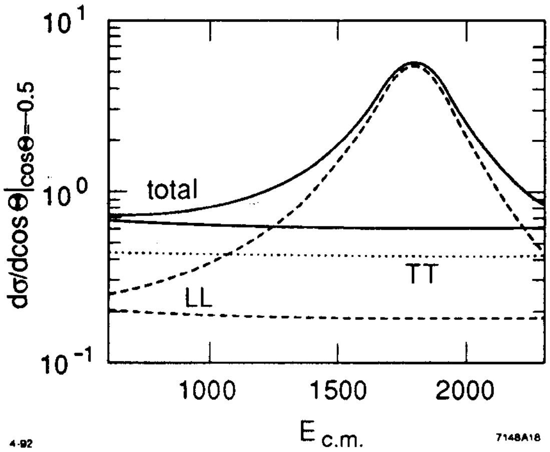

Fig. 18. The effect of a 1.8 TeV techni-ρ resonance in the $W_L^+W_L^- \rightarrow W_L^+W_L^-$ channel on the $e^+e^- \rightarrow W^+W^-$ cross-section.

$W_L^+W_L^- \rightarrow W_L^+W_L^-$, where W_L^- denotes a longitudinally polarized W^- boson. This is discussed, for example, in Refs. 12 and 13. The effect of a 1.8 TeV techni-ρ resonance in the $W_L^+W_L^- \rightarrow W_L^+W_L^-$ channel on the $e^+e^- \rightarrow W^+W^-$ cross-section is shown in Fig. 18. We incorporate this effect into our analysis by multiplying the standard model amplitude for $e^+e^- \rightarrow W_L^+W_L^-$ by the rescattering coefficient F_T defined by

$$F_T \equiv \exp\left[\frac{1}{\pi}\int_0^\infty ds'\delta(s')\left\{\frac{1}{s'-s-i\epsilon} - \frac{1}{s'}\right\}\right]$$

where

$$\delta(s) = \frac{1}{96\pi}\frac{s}{v^2} + \frac{3}{4}\left[\,tanh\left(\frac{M_\rho\Gamma_\rho}{M_\rho^2 - s}\right) + 1\right],$$

v = 240 GeV is the Higgs vacuum expectation value, M_ρ is the techni-ρ mass and Γ_ρ is the techni-ρ width. Fig. 19 shows $\mathrm{R_e(F_T)}$ and $\mathrm{I_m(F_T)}$, the real and

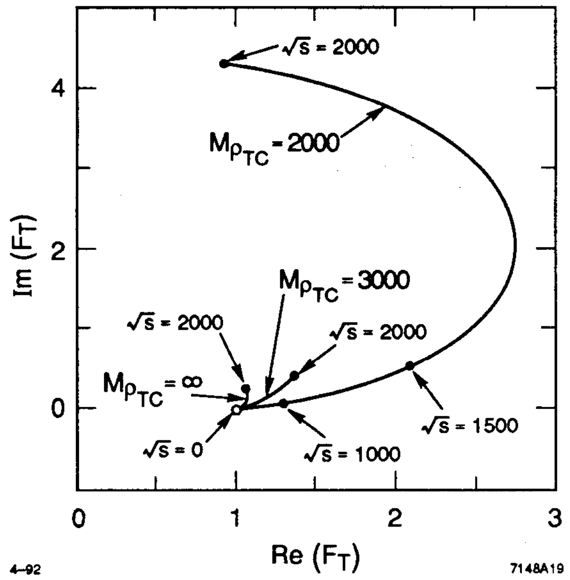

Fig. 19. $\mathrm{I_m}(\mathrm{F_T})$ vs. $\mathrm{R_e}(\mathrm{F_T})$ for three values of the techni-ρ mass M_ρ.

imaginary parts of F_T for three values of the techni-ρ mass M_ρ. The shortest curve corresponds to $M_\rho = \infty$, the longest curve has $M_\rho = 2\ TeV$, and the intermediate curve has $M_\rho = 3\ TeV$. For each curve the values of $\mathrm{R_e}(\mathrm{F_T})$ and $\mathrm{I_m}(\mathrm{F_T})$ are shown from $\sqrt{s} = 0$ to $\sqrt{s} = 2$ TeV.

To assess our sensitivity to $\mathrm{R_e}(\mathrm{F_T})$ and $\mathrm{I_m}(\mathrm{F_T})$ we do another maximum log likelihood analysis. This time we parameterize the log likelihood function with the variables $\mathrm{R_e}(\mathrm{F_T}), \mathrm{I_m}(\mathrm{F_T})$, and $\mathcal{L}$, instead of the variables $\kappa_\gamma, \lambda_\gamma, \kappa_Z, \lambda_Z, \mathcal{L}$. Our log likelihood function $\ln L(\mathrm{R_e}(\mathrm{F_T}), \mathrm{I_m}(\mathrm{F_T}), \mathcal{L})$ is otherwise identical to the the one defined in Eq. (6). For the purpose of this discussion we set the coupling parameters $\kappa_\gamma, \lambda_\gamma, \kappa_Z, \lambda_Z$ equal to their standard model values. We have found, however, that this approximation will not be necessary since the variables $\kappa_\gamma, \lambda_\gamma, \kappa_Z, \lambda_Z, \mathrm{R_e}(\mathrm{F_T}), \mathrm{I_m}(\mathrm{F_T})$ were remarkably orthogonal when simultaneous fits of all 6 variables were performed.

The 95% confidence level contours for $\mathrm{R_e}(\mathrm{F_T})$ and $\mathrm{I_m}(\mathrm{F_T})$ are shown in Fig. 20 for three different e^+e^- center-of-mass energies. At $\sqrt{s} = 1000$ GeV and 1500 GeV we have assumed modest luminosities of 45 fb^{-1} and of 90 fb^{-1}, respectively. We see that at these center-of-mass energies a 1.7 TeV techni-ρ resonance is easily observable. At $\sqrt{s} = 500$ GeV though, and despite the fact that we have assumed a hefty integrated luminosity of of 30 fb^{-1}, the 1.7 TeV techni-ρ is located right on the 95% confidence level contour.

Figs. 21 and 22 show 95% confidence level contours in $\mathrm{R_e}(\mathrm{F_T}), \mathrm{I_m}(\mathrm{F_T})$ space for more aggressive luminosities at $\sqrt{s} = 1000$ GeV . With 200 fb^{-1} (Fig. 21) it appears

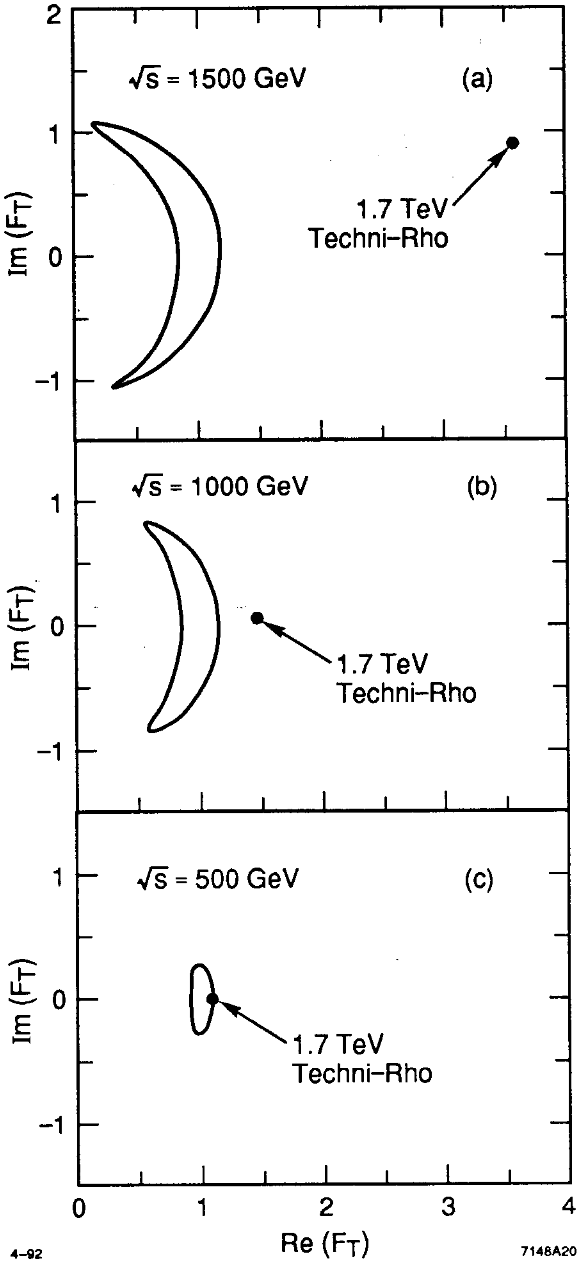

Fig. 20. The 95% confidence level contours for $R_e(F_T)$ and $I_m(F_T)$ for (a) $\sqrt{s} = 1500$, $\mathcal{L} = 90\ fb^{-1}$; (b) $\sqrt{s} = 1000$, $\mathcal{L} = 45\ fb^{-1}$; (c) $\sqrt{s} = 500$, $\mathcal{L} = 30\ fb^{-1}$

possible to detect the presence of a techni-ρ resonance with a mass as large as 4 or 5 TeV. Unfortunately it is not possible at this luminosity to differentiate between a non-resonant strongly interacting Higgs sector and the weakly interacting Higgs sector using this particular technique. In Fig. 22, though, where the luminosity is 2000 fb^{-1}, we see the non-resonant strongly interacting Higgs sector (marked

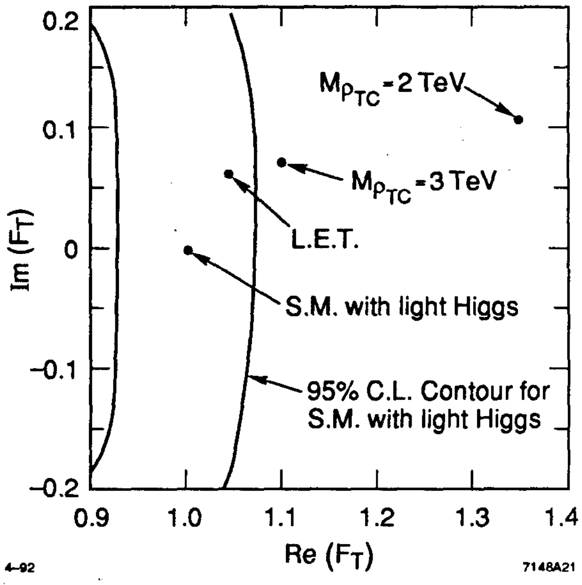

Fig. 21. The 95% confidence level contours for R$_e$(F$_T$) and I$_m$(F$_T$) for $\sqrt{s}$ = 1000, $\mathcal{L} = 200\ fb^{-1}$

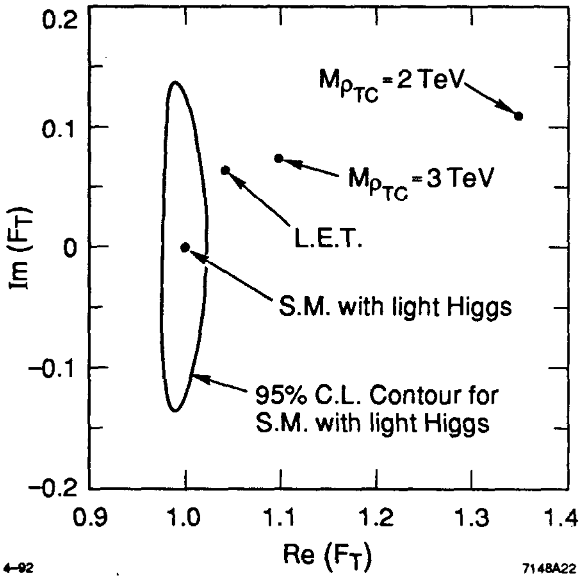

Fig. 22. The 95% confidence level contours for R$_e$(F$_T$) and I$_m$(F$_T$) for $\sqrt{s}$ = 1000, $\mathcal{L} = 2000\ fb^{-1}$

by L.E.T. or Low Energy Theorem) clearly separated from the weakly interacting Higgs sector (the standard model with one or more light Higgs bosons).

It is unfortunate that the integrated luminosity in Fig. 22 is so large. If it were possible to achieve this luminosity then this fit of the $W_L^+W_L^-$ rescattering coefficients $\mathrm{R_e}(\mathrm{F_T})$ and $\mathrm{I_m}(\mathrm{F_T})$ would be the definitive experiment telling us whether the Higgs sector is strongly interacting or weakly interacting. For example, suppose that no light Higgs has been found and that LHC and SSC have not seen any multi-TeV techni-resonances before this experiment is performed. If the experiment is performed and the measured value of $\mathrm{R_e}(\mathrm{F_T})$ and $\mathrm{I_m}(\mathrm{F_T})$ lands inside the 95% confidence level contour, then we might want to go back and look harder for a light Higgs boson. If, on the other hand, $\mathrm{R_e}(\mathrm{F_T})$ and $\mathrm{I_m}(\mathrm{F_T})$ land outside the 95% contour then we would begin to believe that we had not missed a light Higgs boson and that the Higgs sector was indeed strongly interacting.

6. Conclusions

The reactions $e^-\gamma \to \nu W^-$ and $\gamma\gamma \to W^+W^-$ are excellent probes of the $W^+W^-\gamma$ vertex, especially when Compton scattered laser light is used. Limits of $|\kappa_\gamma - 1| < 0.3$ and $|\lambda_\gamma| < 0.06$ can be obtained with 10 fb^{-1} at $\sqrt{s} = 500$ GeV. These limits are independent of κ_Z and λ_Z.

The process $e^+e^- \to W^+W^-$ was investigated extensively, and was found to be an excellent probe of both the $W^+W^-\gamma$ and W^+W^-Z vertices. The parameters $\kappa_\gamma, \lambda_\gamma, \kappa_Z, \lambda_Z$ can be readily disentangled, and 10 fb^{-1} at $\sqrt{s} = 500$ GeV will give us limits of at least

$$|\kappa_\gamma - 1|, |\kappa_Z - 1|, \lambda_\gamma, \lambda_Z < 0.03,$$

with no assumptions about which couplings are held fixed at their standard model values. With higher luminosities these limits should approach 0.01.

Finally, W^+W^- rescattering at $1\ \text{TeV} < \sqrt{s} < 1.5\ \text{TeV}$ will start to probe non-resonant $W_L^+W_L^-$ strong interactions when $\mathcal{L} > 500\ fb^{-1}$, while resonances will be visible at lower luminosities.

Acknowledgments

I have benefitted greatly from conversations with D. Burke, M. Peskin, A. Miyamoto, F. Schrempp, E. Yehudai and R. Settles. This work was supported in part by U.S. Department of Energy contract DE-AC03-76SF00515.

REFERENCES

1. K. Hagiwara, R.D. Peccei, D. Zeppenfeld, and K. Hikasa, *Nucl. Phys.* **B282**, 253 (1987).
2. G.L. Kane, J. Vidal, and C.-P. Yuan, *Phys. Rev.* **D39**, 2617 (1989).
3. A.de Rujula,M.B.Gavela,P. Hernandez, and E.Masso, preprint CERN-TH.6272/91 (1991); K.Hagiwara,S.Ishihara,R.Szalapski, D.Zeppenfeld, preprint MAD/PH/690 (1992).
4. C. Akerlof, University of Michigan Report No. UMHE 81–59, (1981).
5. I.F. Ginzburg *et al.*, *Nucl. Instrum. Methods* **205**, 47 (1983); I.F. Ginzburg *et al.*, *Nucl. Instrum. Methods Phys. Res.* **219**, 5 (1984); V.I. Telnov, Novosibirsk Institute of Nuclear Physics Report No. 89-90, 1989.
6. T. Barklow, in *Proceedings of the 1990 DPF Summer Study on High-Energy Physics: Research Directions for the Decade (Snowmass,Colo.)* and SLAC-PUB-5364.
7. E. Yehudai, *Phys. Rev.* **D41**, 33 (1990).
8. S.Y.Choi and F.Schrempp, preprint DESY 91-155 (1991).
9. E. Yehudai, SLAC Report No. 383 (1991).
10. E. Yehudai, *Phys. Rev.* **D44**, 3434 (1991).
11. D. Hitlin *et al.*, SLAC Report No. 273 (1984).
12. M.E.Peskin, in *Physics in Collision 4*, A.Seiden, ed. (Editions Frontieres, Gif-sur-Yvette, 1984).
13. K.Hikasa, plenary talk at this workshop and preprint KEK-TH-319 (1992)